IEEE Open Journal of
Antennas and Propagation

Received 28 January 2023; revised 3 March 2023; accepted 9 March 2023. Date of publication 15 March 2023; date of current version 27 March 2023.

Digital Object Identifier 10.1109/OJAP.2023.3257355

Additively-Manufactured All-Dielectric Microwave Polarization Converters Using Ceramic Stereolithography

STEVE M. YOUNG[1] (Member, IEEE), MARK KAUF[2], JEFFREY KUTSCH[2], AND ANTHONY GRBIC[1] (Fellow, IEEE)

[1]Department of Electrical and Computer Engineering, University of Michigan, Ann Arbor, MI 48109, USA

[2]Additive Manufacturing Department, Technology Assessment and Transfer, Inc., Millersville, MD 21401, USA

CORRESPONDING AUTHOR: S. M. YOUNG (e-mail: yms@umich.edu)

This work was supported by the Air Force Office of Scientific Research under Grant FA9550-18-1-0466.

ABSTRACT We report a class of all-dielectric, additively-manufactured polarization converters with tailored temporal frequency responses within the Ku and Ka microwave bands (15 – 40 GHz). These multi-layer devices consist of cascaded, subwavelength, high-contrast gratings with different fill fractions and orientations, providing control over the effective anisotropic properties of each layer. In design, the subwavelength gratings are modeled as homogeneous anisotropic layers. This allows the overall metastructure to be treated as a stratified dielectric medium. Therefore, it can be analyzed and optimized using plane-wave transfer matrix techniques that fully account for multiple reflections between layers. Using this cascaded grating geometry, a variety of high-efficiency microwave polarization converters can be realized with broadband, multiband, or multifunctional behavior. The transmissive metastructures do not require anti-reflection layers since impedance matching is incorporated into their design. Three example devices based on alumina/air gratings have been monolithically fabricated using ceramic stereolithography: a broadband reflective half-wave plate, a broadband isotropic polarization rotator, and a dual-band linear-to-circular polarization converter.

INDEX TERMS Antennas, birefringence, ceramics, dielectric devices, gratings, metamaterials, metasurfaces, microwave devices, nonhomogeneous media, polarization, stereolithography, three-dimensional printing.

I. INTRODUCTION

IT HAS long been known that cascaded, rotated, birefringent slabs can provide polarization conversion with tailored spectral responses [1], which has been used to design a variety of optical devices [2] including broadband waveplates for Terahertz [3] and submillimeter wave [4] applications. Conventionally, such devices have comprised naturally occurring birefringent materials. However, this principle can be extended by cascading subwavelength dielectric gratings exhibiting structural birefringence [5], [6], [7] to enable increased control over the effective anisotropic properties of each layer.

In particular, a one-dimensional dielectric grating with period Λ much smaller than the free space wavelength λ_0, as illustrated in Fig. 1, can be treated as a uniaxial homogeneous slab [5], [7], [8] with permittivities

$$\frac{1}{\epsilon_\perp} = \frac{f}{\epsilon_1} + \frac{1-f}{\epsilon_2} + O\Big((\Lambda/\lambda_0)^2\Big), \tag{1}$$

$$\epsilon_\parallel = f\epsilon_1 + (1-f)\epsilon_2 + O\Big((\Lambda/\lambda_0)^2\Big), \tag{2}$$

where $\epsilon_\perp$ and $\epsilon_\parallel$ are the effective permittivity along the grating's extraordinary and ordinary optic axes, and f is the filling ratio of medium 1.

Numerous examples of simple polarization devices using subwavelength gratings have been demonstrated including achromatic quarter-wave plates [9], [10], [11], half-wave plates [12], and anti-reflection coatings [13]. More exotic

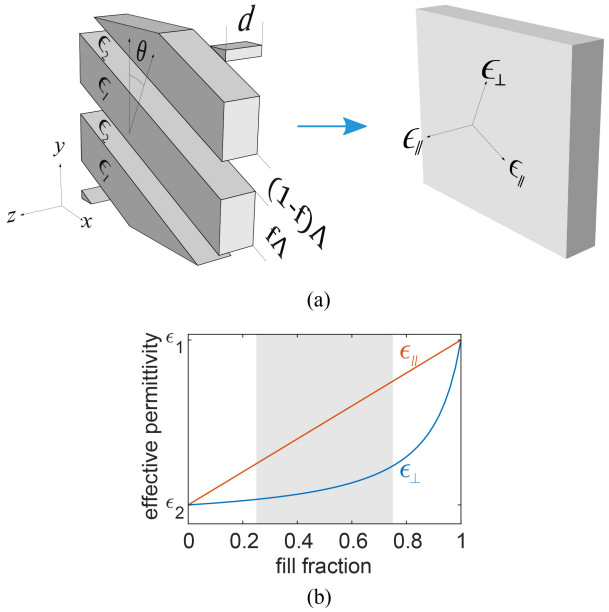

FIGURE 1. (a) A subwavelength grating layer and its equivalent anisotropic slab with permittivities $\epsilon_\perp$ and $\epsilon_\parallel$. (b) Representative values of effective permittivities $\epsilon_\perp$ and $\epsilon_\parallel$, as a function of filling fraction, for a subwavelength grating of materials ϵ_1 and ϵ_2. The gray shaded region indicates a typical realizable range of filling fractions.

broadband, multiband, and multifunctional polarization converters have also been proposed using more complex structures with cascaded and rotated dielectric elements [14], [15], [16].

However, devices based on cascaded subwavelength gratings pose significant fabrication challenges, especially if the grating layers are rotated with respect to each other. One approach is to individually manufacture each grating layer using a lithographic process, then precisely assemble the layers in the correct orientation as done in [16] with etched silicon/air grating layers. Another example is the broadband linear-to-circular polarizer in [17], which used cascaded artificial dielectrics assembled from printed circuit boards rather than subwavelength gratings.

In this work, we explore the design and fabrication of cascaded subwavelength grating structures using an additive manufacturing process (ceramic stereolithography) to enable monolithic fabrication without a separate assembly step. In ceramic stereolithography [18], [19], [20], [21], [22], [23], [24], [25], [26], [27], an ultraviolet light source is used to selectively cure a photoreactive ceramic particle suspension layer-by-layer, resulting in a "green" part that is subsequently pyrolyzed and sintered to remove polymer components and leave a pure, dense ceramic structure. The process can produce high accuracy parts with small, high-contrast features that are well-suited to subwavelength patterning at microwave frequencies. It has been used to fabricate isotropic effective media in graded-index Ka-band devices [28].

In this article, we describe the design, fabrication, and measurement of all-dielectric polarization converters using ceramic stereolithography. Full wave simulations of

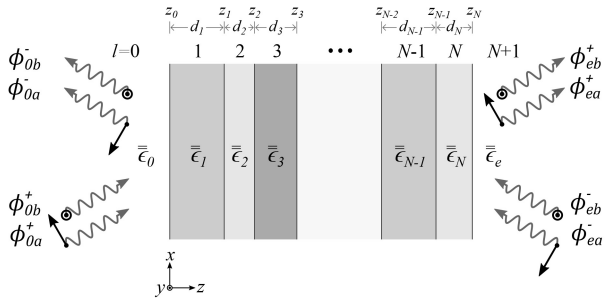

FIGURE 2. Plane wave obliquely incident on a stratified slab consisting of N uniform layers, each characterized by thickness d_l and 3 × 3 permittivity tensor $\bar{\bar{\epsilon}}_l$.

these structures, which consist of multiple cascaded and rotated subwavelength gratings, can be prohibitively complex. However, suitable homogenization assumptions allow for a fast, semi-analytic analysis method based on transfer matrix techniques, which in turn enables rapid numeric optimization for a given desired polarization conversion. The ceramic stereolithography fabrication procedure and measurement techniques will be discussed. Finally, three fabricated example devices will be presented with a comparison of their analytic and measured performance.

The structures in this work will be treated as having transversely-homogeneous, but longitudinally-variable material properties. They can be contrasted with the related class of transversely-inhomogeneous and longitudinally-uniform effective medium slabs, which can be used to implement blazed gratings [29] and phase plates [30], for example.

II. ANALYSIS AND DESIGN METHOD

A structure with three or more rotated, cascaded, gratings of the sort shown in Fig. 1, whose principle axes do not align, cannot in general be rigorously simulated using a single unit cell of a periodic lattice. However, a simple and exact solution is possible provided each grating can be represented by an equivalent homogeneous medium. We assume that the field at the boundary between two gratings is well-represented by the fundamental Floquet modes, and that evanescent coupling does not significantly affect the polarization converter's response. For deeply subwavelength gratings with $\Lambda/\lambda_0 < 0.1$, we apply the effective medium relations (1) and (2) to obtain the piecewise-uniform stratified structure shown in Fig. 2. Each grating layer is treated as a nonmagnetic, uniaxial, homogeneous medium with principal axes rotated by an angle θ_l in the $xy-$plane. The constitutive relation in each layer is then:

$$\begin{pmatrix} \epsilon_0\bar{\bar{\epsilon}} & \mathbf{0} \\ \mathbf{0} & \mu_0\boldsymbol{I} \end{pmatrix}\begin{pmatrix} \boldsymbol{E} \\ \boldsymbol{H} \end{pmatrix} = \begin{pmatrix} \boldsymbol{D} \\ \boldsymbol{B} \end{pmatrix} \tag{3}$$

where $\boldsymbol{I}$ is the 3×3 identity matrix, and $\bar{\bar{\boldsymbol{\epsilon}}}$ is given by:

$$\bar{\bar{\boldsymbol{\epsilon}}} = \begin{pmatrix} \epsilon_{xx} & \epsilon_{xy} & 0 \\ \epsilon_{yx} & \epsilon_{yy} & 0 \\ 0 & 0 & \epsilon_{zz} \end{pmatrix}$$

$$= \begin{pmatrix} \epsilon_\parallel \cos^2\theta_l + \epsilon_\perp \sin^2\theta_l & (\epsilon_\parallel - \epsilon_\perp)\cos\theta_l \sin\theta_l & 0 \\ (\epsilon_\parallel - \epsilon_\perp)\cos\theta_l \sin\theta_l & \epsilon_\parallel \sin^2\theta_l + \epsilon_\perp \cos^2\theta_l & 0 \\ 0 & 0 & \epsilon_\parallel \end{pmatrix} \quad (4)$$

Within this homogenization assumption, in which higher-order Floquet harmonics are neglected, 4×4 matrix techniques [31], [32], [33], [34] are sufficient to exactly and rapidly compute plane-wave reflection and transmission through the structure, including polarization conversion and reflections between layers. A wide range of desired responses can then be achieved by numerically optimizing three parameters per layer: filling fraction f_l, layer thickness d_l, and optic axis rotation angle θ_l [16].

A. TRANSFER MATRIX ANALYSIS

The 4×4 matrix technique [31], [32], [33], [34] provides an exact solution for plane wave transmission through piecewise-homogeneous, stratified media. This section describes a special case of the 4×4 matrix technique for nonmagnetic anisotropic media that is well-suited for rapidly analyzing cascaded subwavelength gratings.

Considering monochromatic fields with $\exp(i\omega t)$ time evolution, in Cartesian coordinates, Faraday's and Ampere's Laws in source-free media can be written in a matrix form:

$$\begin{pmatrix} \mathbf{0} & \nabla\times \\ -\nabla\times & \mathbf{0} \end{pmatrix} \begin{pmatrix} \boldsymbol{E} \\ \boldsymbol{H} \end{pmatrix} = i\omega \begin{pmatrix} \boldsymbol{D} \\ \boldsymbol{B} \end{pmatrix} \quad (5)$$

Since the material properties depend only on z, plane wave fields have the form $\boldsymbol{A}(z)e^{-ik_x x}e^{-ik_y y}e^{i\omega t}$ and the curl operator has the form:

$$\nabla\times = \begin{pmatrix} 0 & -\frac{\partial}{\partial z} & -ik_y \\ \frac{\partial}{\partial z} & 0 & ik_x \\ ik_y & -ik_x & 0 \end{pmatrix} \quad (6)$$

Combining (3), (5), and (6) yields a system of six equations, of which the third and sixth are linear algebraic equations relating the six components of $\boldsymbol{E}$ and $\boldsymbol{H}$. These can be solved for E_z and H_z in terms of the other four components, yielding the following 4×4 wave equation for the transverse fields:

$$\frac{\partial}{\partial z} \begin{pmatrix} E_x \\ E_y \\ H_x \\ H_y \end{pmatrix} = -ik_0 \boldsymbol{\Lambda} \begin{pmatrix} E_x \\ E_y \\ H_x \\ H_y \end{pmatrix} \quad (7)$$

In the previous equation, $k_0 = \omega/c$ is the free space wavenumber and $\boldsymbol{\Lambda}$ is a 4×4 matrix with the following block diagonal form:

$$\boldsymbol{\Lambda} = \begin{pmatrix} \mathbf{0} & \boldsymbol{\Lambda}_{EM} \\ \boldsymbol{\Lambda}_{ME} & \mathbf{0} \end{pmatrix} \quad (8)$$

$$\boldsymbol{\Lambda}_{EM} = \eta_0 \begin{pmatrix} k_x k_y/(k_0^2\epsilon_{zz}) & 1 - k_x^2/(k_0^2\epsilon_{zz}) \\ -1 + k_y^2/(k_0^2\epsilon_{zz}) & -k_x k_y/(k_0^2\epsilon_{zz}) \end{pmatrix} \quad (9a)$$

$$\boldsymbol{\Lambda}_{ME} = \frac{1}{\eta_0} \begin{pmatrix} -\epsilon_{yx} - k_x k_y/k_0^2 & -\epsilon_{yy} + k_x^2/k_0^2 \\ \epsilon_{xx} - k_y^2/k_0^2 & \epsilon_{yx} + k_x k_y/k_0^2 \end{pmatrix} \quad (9b)$$

where $\eta_0 = \sqrt{\mu_0/\epsilon_0}$ is the free-space wave impedance.

Noting that the structure is piecewise uniform and the material properties do not depend on z within each layer, (7) has four solutions for the total transverse field vector $\boldsymbol{\psi_l} = (E_x, E_y, H_x, H_y)$ of the form

$$\boldsymbol{\psi_{ln}}(z_0 + \delta z) = e^{-jq_{ln}k_0\delta z}\boldsymbol{\psi_{ln}}(z_0), \qquad n = 1, 2, 3, 4 \quad (10)$$

which when substituted in eq. (7) yields the eigenvalue equation:

$$q_{ln}\boldsymbol{\psi_{ln}} = \boldsymbol{\Lambda_l}\boldsymbol{\psi_{ln}} \quad (11)$$

Equation (11) can be solved numerically for each layer to find the four characteristic propagation constants q_{ln} and associated eigenmodes $\boldsymbol{\psi_{ln}}$. In general, the total transverse field $\boldsymbol{\psi_l}$ at a given position z within the structure can be decomposed into a weighted superposition of the eigenmodes with weights $\boldsymbol{\phi_l} = (\phi_1, \phi_2, \phi_3, \phi_4)^T$. The total field and mode amplitudes are related by:

$$\boldsymbol{\psi_l}(z) = \boldsymbol{A_l}\boldsymbol{\phi_l}(z) \quad (12)$$

where $\boldsymbol{A_l} = (\boldsymbol{\psi_{l1}}, \boldsymbol{\psi_{l2}}, \boldsymbol{\psi_{l3}}, \boldsymbol{\psi_{l4}})$ is a weighting matrix whose columns are the eigenmodes of $\boldsymbol{\Lambda_l}$. The eigenmodes propagate within each layer according to:

$$\boldsymbol{\phi_l}(z) = \boldsymbol{K_l^-}\boldsymbol{\phi_l}(z + d) \quad (13)$$

with a diagonal propagation matrix $\boldsymbol{K_l^-}$:

$$\boldsymbol{K_l^-} = \begin{pmatrix} e^{iq_{l1}k_0 d} & 0 & 0 & 0 \\ 0 & e^{iq_{l2}k_0 d} & 0 & 0 \\ 0 & 0 & e^{iq_{l3}k_0 d} & 0 \\ 0 & 0 & 0 & e^{iq_{l4}k_0 d} \end{pmatrix} \quad (14)$$

Finally, by combining (12) and (13) and enforcing that the transverse fields must match across each layer boundary, a wave matrix $\boldsymbol{W}$ can be constructed relating the mode amplitudes on the incident ($z = z_0$) and exit ($z = z_N$) edges of the cascaded structure. Ordering the modes in the incident and exit media according to their polarization and propagation direction as depicted in Fig. 2,

$$\begin{pmatrix} \phi_{0a}^+ \\ \phi_{0b}^+ \\ \phi_{0a}^- \\ \phi_{0b}^- \end{pmatrix} = \boldsymbol{A_0}^{-1} \prod_{l=1}^{N} \left(\boldsymbol{A_l}\boldsymbol{K_l^-}(d_l)\boldsymbol{A_l}^{-1} \right) \boldsymbol{A_e} \begin{pmatrix} \phi_{ea}^+ \\ \phi_{eb}^+ \\ \phi_{ea}^- \\ \phi_{eb}^- \end{pmatrix} = \begin{pmatrix} \boldsymbol{W_{11}} & \boldsymbol{W_{12}} \\ \boldsymbol{W_{21}} & \boldsymbol{W_{22}} \end{pmatrix} \begin{pmatrix} \phi_{ea}^+ \\ \phi_{eb}^+ \\ \phi_{ea}^- \\ \phi_{eb}^- \end{pmatrix} \quad (15)$$

where the operator Π represents an ordered product with largest l values to the right.

The transmission and reflection coefficients for the cascaded structure are most conveniently represented by the scattering matrix $\boldsymbol{S}$, which relates scattered to incident mode amplitudes. The scattering matrix can be obtained from the

wave matrix as follows [34]:

$$\begin{pmatrix} \phi_{0a}^{-} \\ \phi_{0b}^{-} \\ \phi_{ea}^{+} \\ \phi_{eb}^{+} \end{pmatrix} = \begin{pmatrix} \boldsymbol{S_{11}} & \boldsymbol{S_{12}} \\ \boldsymbol{S_{21}} & \boldsymbol{S_{22}} \end{pmatrix} \begin{pmatrix} \phi_{0a}^{+} \\ \phi_{0b}^{+} \\ \phi_{ea}^{-} \\ \phi_{eb}^{-} \end{pmatrix} = \begin{pmatrix} \boldsymbol{0} & \boldsymbol{W_{11}} \\ \boldsymbol{-I} & \boldsymbol{W_{21}} \end{pmatrix}^{-1} \begin{pmatrix} \boldsymbol{I} & \boldsymbol{-W_{12}} \\ \boldsymbol{0} & \boldsymbol{-W_{22}} \end{pmatrix} \begin{pmatrix} \phi_{0a}^{+} \\ \phi_{0b}^{+} \\ \phi_{ea}^{-} \\ \phi_{eb}^{-} \end{pmatrix} \quad (16)$$

The preceding analysis is valid for plane waves of arbitrary polarization and incidence angle. In the special case of normal incidence, with $k_x, k_y = 0$, the wave equation (7) takes a simple form with $\boldsymbol{\Lambda}$ given by:

$$\boldsymbol{\Lambda}(k_x, k_y = 0) = \begin{pmatrix} 0 & 0 & 0 & \eta_0 \\ 0 & 0 & -\eta_0 & 0 \\ -\epsilon_{yx}/\eta_0 & -\epsilon_{yy}/\eta_0 & 0 & 0 \\ \epsilon_{xx}/\eta_0 & \epsilon_{xy}/\eta_0 & 0 & 0 \end{pmatrix} \quad (17)$$

The eigenmodes at normal incidence are linearly polarized along the grating's principal axes, with $q_1 = \sqrt{\epsilon_{\parallel}}$, $q_2 = \sqrt{\epsilon_{\perp}}$, $q_3 = -\sqrt{\epsilon_{\parallel}}$, and $q_4 = -\sqrt{\epsilon_{\perp}}$. The associated eigenmode matrix $\boldsymbol{A_l}$ is then given by:

$$\boldsymbol{A_l}(k_x, k_y = 0) = \begin{pmatrix} \cos\theta_l & -\sin\theta_l & -\cos\theta_l & -\sin\theta_l \\ \sin\theta_l & \cos\theta_l & -\sin\theta_l & \cos\theta_l \\ -\sin\theta_l/\eta_{\parallel} & -\cos\theta_l/\eta_{\perp} & -\sin\theta_l/\eta_{\parallel} & \cos\theta_l/\eta_{\perp} \\ \cos\theta_l/\eta_{\parallel} & -\sin\theta_l/\eta_{\perp} & \cos\theta_l/\eta_{\parallel} & \sin\theta_l/\eta_{\perp} \end{pmatrix} \quad (18)$$

where $\eta_{\parallel} = \eta_0/\sqrt{\epsilon_{\parallel}}$ and $\eta_{\perp} = \eta_0/\sqrt{\epsilon_{\perp}}$ are the wave impedances along the principal grating axes.

B. DESIGN SYNTHESIS AND OPTIMIZATION

Given the grating parameters for each layer (grating materials, filling fraction f_l, layer thickness d_l and optic axis rotation angle θ_l), the transfer matrix analysis method in the previous section allows computing the scattering matrix extremely quickly by simply multiplying several 4×4 matrices. Thus, the computation can be included within the cost function for a numerical optimization to obtain a wide range of polarization and spectral responses, including broadband, multiband, and multifunctional devices. Section V describes three fabricated design examples.

III. FABRICATION

To maximize the range of achievable anisotropic effective permittivities, the subwavelength gratings should be constructed from materials with a large permittivity contrast. In this work, we demonstrate additively manufactured devices consisting of alumina (Al_2O_3, $\epsilon_1 = 9.7$) and air ($\epsilon_2 = 1$) which are well-suited for microwave frequencies due to their high dielectric contrast and low loss [35], [36].

The stacked grating structures are fabricated using a ceramic stereolithography additive manufacturing process. A resin is prepared consisting of sinterable alumina powder and a mixture of photopolymerizable monomers, dispersants, photoinitiators and photoabsorbers. The resin is photocured layer-by-layer as in conventional stereolithography to produce a green state part, which is then thermally processed to remove the binder, and sintered. During sintering the part shrinks volumetrically in a predictable manner by approximately 19%, which is compensated by scaling the design appropriately. After processing, the remaining alumina has a purity of 98% and density greater than 97%, with $\epsilon_1 = 9.7$ and estimated loss tangent $\tan\delta_1 = 10^{-4}$.

Numerous prototypes of all-dielectric polarization converters designed for operation in the Ku to Ka microwave bands were additively manufactured by Technology Assessment & Transfer, Inc. (TA&T, Millersville, MD) using an alumina-filled resin formulation on an industrial scale DLP 3D printer. The vat-based printing process utilizes a 365 nm LED-based light source to polymerize the filled resin layer-by-layer. The system is capable of printing at a cured resin resolution of 42 μm x 42 μm in the x-y build plane and as small as 10 μm in the z-plane (layer thickness). Layer thicknesses less than 50 μm often increase build times without adding practical structural or geometric benefits to parts. Therefore, a layer thickness of 50 μm was chosen for these builds resulting in an 8.8×10^{-4} mL cured or 4.1×10^{-4} mL sintered voxel resolution. The printer is fitted with vat and build platform with a 250 mm x 250 mm x 150 mm build volume, which translates into dense alumina parts up to 190 mm x 190 mm x 115 mm in overall dimension. The system is capable of producing parts within a much larger volume (7–10 times more) when appropriate machine accessories are installed.

The vat-based printer builds a single layer of the part by exposing a 50 μm thick layer of resin on the build platform to a projected UV light source. Once a layer is cured the build platform lowers by a layer thickness of 50 μm into the resin vat and a sweeping or suction blade moves across the build platform and deposits the next layer to be cured. The printer repeats this process until the parts are fully formed.

Due to the geometrical complexity of the polarization converters, careful consideration was made to determine optimal printing orientation. The ideal orientation would minimize the sweeping blade shear forces applied to the thinnest and tallest metastructure struts by having those as close to perpendicular to the blade as possible or parallel to the sweep direction (see Fig. 3).

Furthermore, design alterations were made to the CAD model to enable the final printed part to accurately scale to the desired dimensions. These alterations included shrinking the strut wall widths on the varying levels to account for light scattering, a phenomenon inherently present in ceramic suspension photopolymerization. Light scattering causes the light source to be projected laterally as it hits the ceramic suspension, thereby slightly increasing the final dimensions of the walls in the x-y plane. The degree to which this effect occurs depends on the refractive index of the resin and the energy dosage emitted from the light source.

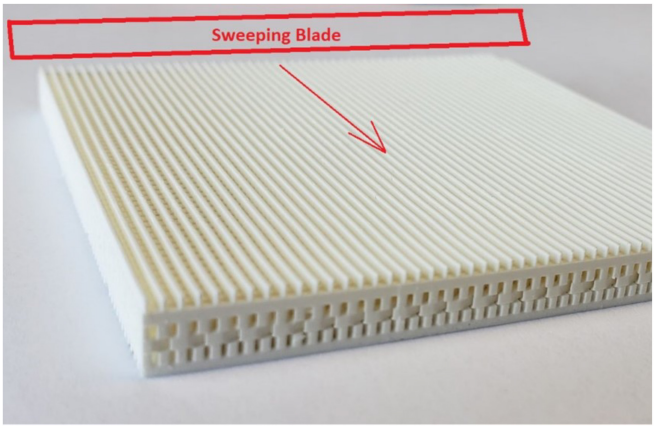

FIGURE 3. Optimized antenna orientation relative to sweeping blade. Tallest and thinnest layer of struts (top layer) oriented perpendicular to blade to minimize stress and breakages.

Upon completion of the print, the 3D printed structure was carefully removed from the platform and cleaned of excess resin. It is worth noting that because of the extremely narrow passageways, tight channels, and microscopic voids inherent in the cascaded grating structures, a low viscosity shear-thinning resin was used to facilitate effective cleaning. Once fully cleaned, the metastructure was inspected for dimensional accuracy and build quality and subsequently processed through binder burnout and sintering in air atmosphere. The binder burnout was a two-step process and went through an initial low-temperature burnout in a lab oven followed by a bisque firing in a silicon-controlled rectifier (SCR) kiln. The metastructure was supported on porous setting furniture to allow for proper removal of organics. The binder burnout protocol utilized ramp rates of 5–60 °C/h and numerous dwells to volatize the cured resin without damaging the part. Upon completion of the binder burnout, the bisque fired metastructure was transferred to a high temperature furnace where it reached a maximum sintering temperature of 1550 °C which consequently fully densified the metastructure, achieving between 97% – 99.9% total densification as measured by Archimedes' method.

Grating periods of approximately 1 mm, with filling fractions ranging between $0.3 < f < 0.65$ were readily achievable while maintaining structural integrity during processing and allowing uncured resin to be cleaned from the structures. Given these design rules, operating frequencies in the Ka band (26 – 40 GHz) are expected to be possible while maintaining subwavelength feature sizes at the highest frequencies, $\Lambda/\lambda_0 < 0.13$.

IV. MEASUREMENT METHODS

The plane wave reflection and transmission coefficients for the fabricated devices were measured using free-space quasi-optical techniques [17], [37], [38]. Linearly-polarized horn antennas were combined with focusing optics to produce a collimated source focused at the device surface. Measurements in the Ka microwave band (26.5–40 GHz)

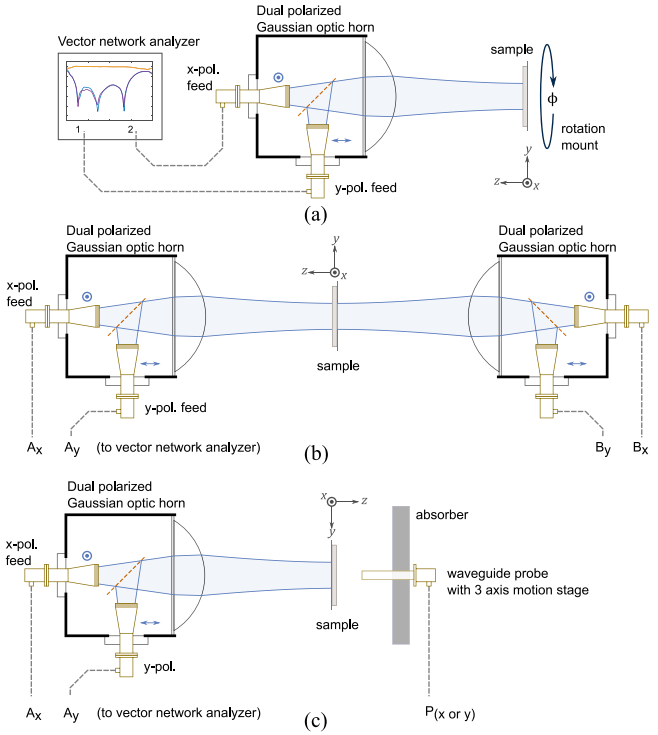

FIGURE 4. Quasi-optical measurement methods for microwave polarization conversion devices (a) Reflection measurement with dual-polarized Gaussian optic horn antenna. (b) Transmission measurement with two dual-polarized Gaussian optic horn antennas. (c) Transmission measurement with probe-compensated near-field scanning and Gaussian optic source.

used dual-polarized antennas with integrated Gaussian optic focusing lenses (Millitech GOA-28), producing a 3 cm beamwaist diameter at a 22 cm distance from the lens. The lower frequency Ku band measurements (17–26.5 GHz) used a standard gain horn antenna with a pair of bi-hyberbolic Rexolite ($n = 1.45$) lenses forming a telescope with 45 cm input and output focal distances [38]. To avoid diffraction effects, the polarization converting devices were fabricated with lateral extent at least three times the beamwaist diameter at the lowest measurement frequency.

The transmitting and receiving horn antennas for each polarization were connected to the four ports of a Keysight E8361A network analyzer with N4421B test set, which collected the transmission and reflection data. Three measurement configurations were used, as illustrated in Fig. 4. For reflective devices, only a single dual-polarized antenna was needed. For transmissive devices, two identical sets of antennas and focusing optics were used to collect the full polarimetric S-parameter data. Finally, probe-compensated near-field scanning [39], [40], [41] was used as an alternative measurement method for transmissive devices. As in the other quasi-optical configurations, one side of the device was illuminated with a focused collimated source. A waveguide probe was then scanned in a grid on the other side of the device using a 3-axis motion stage with 5 μm accuracy, from which the device's far-field transmitted pattern could be reconstructed.

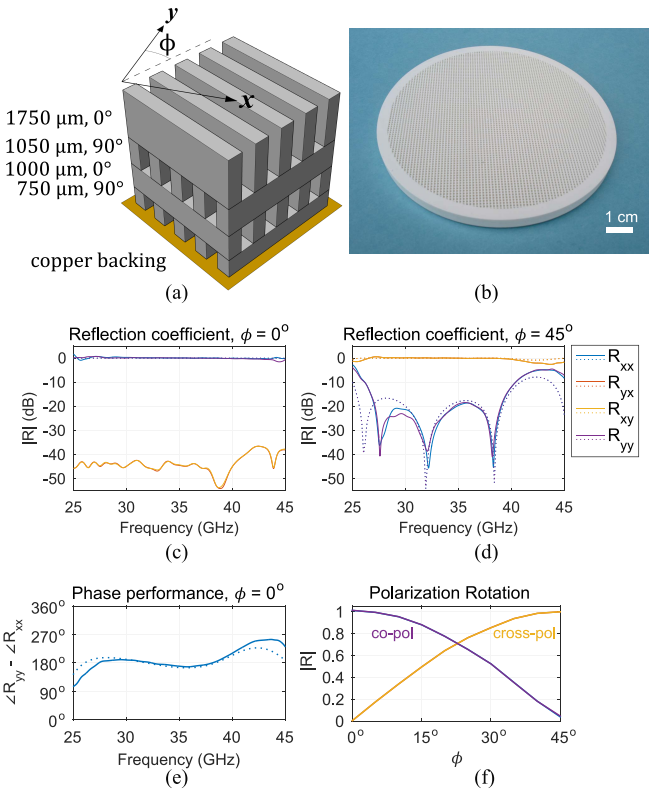

FIGURE 5. **(a) Half-wave plate design and measurement configuration. Excitation is at normal incidence with linear polarization along *x* and *y*. The waveplate's fast optic axis is rotated by an angle ϕ to the *y* axis. (b) Fabricated waveplate (copper backing not shown). (c) Measured (solid) and analytically calculated (dotted) reflection coefficients with $\phi = 0°$. (d) Measured (solid) and calculated (dotted) reflection coefficients with $\phi = 45°$. (e) Measured (solid) and calculated (dotted) phase performance with $\phi = 0°$. Optimal is $\angle R_{yy} - \angle R_{xx} = 180°$. (f) Polarization rotation at 33 GHz as a function of waveplate angle ϕ.**

TABLE 1. **Physical parameters for the Ka-band half-wave plate.**

Symbol	Parameter	Value
ϵ_1	Al_2O_3 permittivity	$9.7(1 - i10^{-4})$
ϵ_2	air permittivity	1
Λ	grating period	1000 μm
N	number of layers	4
d	overall thickness	4.53 mm
d_l	layer thickness	(1750, 1050, 1000, 725) μm
f_l	layer filling fraction	(0.50, 0.50, 0.50, 0.50)
θ_l	layer rotation	(0°, 90°, 0°, 90°)

V. EXAMPLE DEVICES

A. BROADBAND HALF-WAVE PLATE

The first design example, which has been previously reported in [42], is a reflective half-wave plate operating in the Ka band (26.5 – 40 GHz) and fabricated using ceramic stereolithography with alumina and air subwavelength gratings backed by a copper plate. The desired reflection tensor for a half-wave plate is:

$$\begin{pmatrix} E_x^- \\ E_y^- \end{pmatrix} = \boldsymbol{S_{11}} \begin{pmatrix} E_x^+ \\ E_y^+ \end{pmatrix} = e^{i\varphi} \begin{pmatrix} 1 & 0 \\ 0 & -1 \end{pmatrix} \begin{pmatrix} E_x^+ \\ E_y^+ \end{pmatrix} \tag{19}$$

where φ is an arbitrary constant phase shift.

For simplicity, a filling fraction $f_l = 0.5$ was fixed for each layer, with grating period $\Lambda = 1000\,\mu$m to give $\Lambda/\lambda_0 < 0.13$. The layer thicknesses d_l and optic axis rotation angles θ_l were numerically optimized to minimize the difference between the desired (19) and analytically calculated reflection tensors over the operating band. Using more layers widens the bandwidth at the cost of more complexity. In the end, four layers were chosen as a reasonable tradeoff to yield the design shown in Fig. 5(a). The fabricated waveplate is a disk approximately 9 cm in diameter with physical parameters summarized in Table 1.

The co- and cross-polarized reflection performance was measured in the 25 – 45 GHz range using the reflective configuration shown in Fig. 4(a). The waveplate was placed at the focal plane and illuminated at normal incidence. A rotation mount was used to adjust the angle ϕ of the fast optic axis (Fig. 5(a)), and the reflection tensor was measured. Fig. 5 shows the measured waveplate performance. It demonstrates the expected half-wave plate polarization performance and low loss over the entire 26.5 – 40 GHz operating band, as well as excellent agreement between the analytic predictions and measurements.

B. ISOTROPIC ROTATOR

The second design example is a polarization rotator, proposed in [43]. The isotropic rotator is ideally characterized by the transmission tensor:

$$\begin{pmatrix} E_{ex}^+ \\ E_{ey}^+ \end{pmatrix} = \boldsymbol{S_{21}} \begin{pmatrix} E_{0x}^+ \\ E_{0y}^+ \end{pmatrix} = e^{i\varphi} \begin{pmatrix} \cos\alpha & -\sin\alpha \\ \sin\alpha & \cos\alpha \end{pmatrix} \begin{pmatrix} E_{0x}^+ \\ E_{0y}^+ \end{pmatrix} \tag{20}$$

where φ is an arbitrary constant phase shift. That is, linearly-polarized incident light is transmitted without reflection or absorption, and the transmitted polarization is rotated counterclockwise by an angle α. In contrast to the half-wave plate (Section V-A), which can rotate only specific linear polarizations, the isotropic polarization rotator produces the same rotation angle regardless of the incident polarization. Isotropic rotation is an inherently chiral response and is therefore a more demanding design challenge than the half-wave plate [44], [45], [46].

Previously reported isotropic rotators, implemented using chiral or bianisotropic structures [44], [45], [46], have tended to have narrow operating bandwidths. The goal for this example was to achieve a wider bandwidth by exploiting the greater degrees of freedom in a cascaded grating structure. The example rotator was designed to provide $\alpha = 90°$ rotation from 30 – 35 GHz within the Ka band, again using alumina and air subwavelength gratings. The grating period was fixed at $\Lambda = 1100\,\mu$m, while the filling fraction f_l, layer thicknesses d_l and optic axis rotation angles θ_l for each layer were numerically optimized to minimize the difference between the desired (20) and analytically-calculated transmission tensors over the operating band. The optimized and fabricated device comprises 9 layers with overall thickness 10.0 mm, with physical parameters summarized in Table 2.

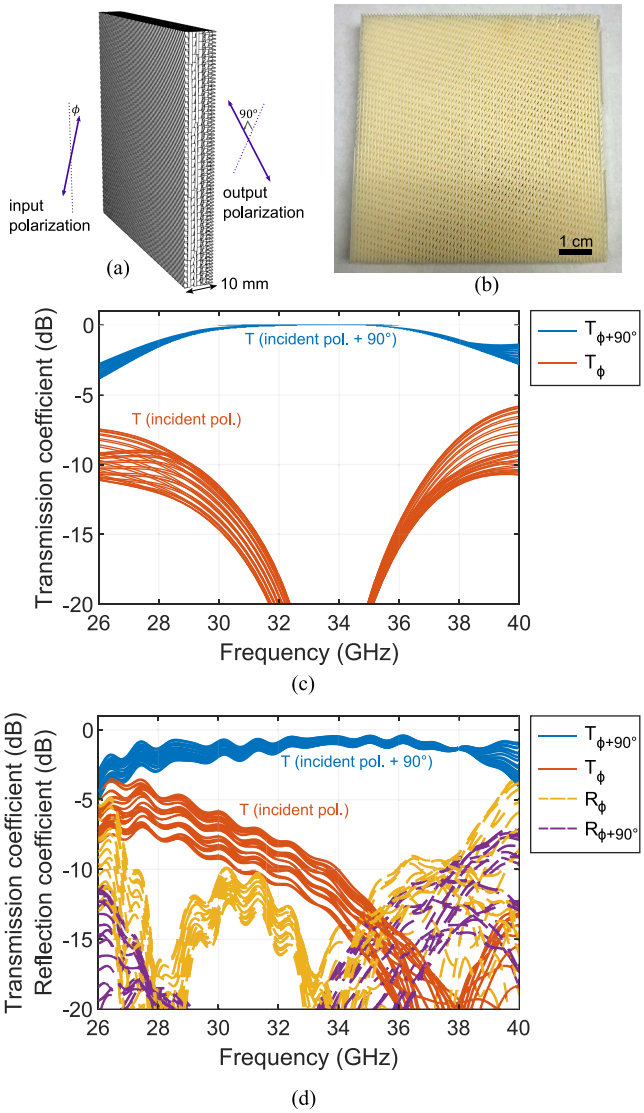

FIGURE 6. (a) Isotropic 90° polarization rotator design and illustration of operating characteristics. Linearly polarized incident light is transmitted without reflection or absorption, and the transmitted polarization is rotated counterclockwise by 90°. (b) Fabricated device. (c) Calculated transmission into the rotated (blue) and incident (red) polarizations using the analytic 4 × 4 matrix technique. Each curve represents a different incidence polarization angle between 0° and 180°. (d) Measured transmission (solid) and reflection (dashed) coefficients for the incident and rotated polarizations.

The polarization rotation performance was measured in the 26 – 40 GHz range using the transmissive configuration shown in Fig. 4(b). To confirm the device's isotropic behavior, a rotation mount was used to adjust the incident polarization angle in 10° increments from 0° to 180°. Fig. 6 shows the analytically-predicted and measured performance for each incident polarization. The desired broadband polarization rotation behavior was achieved, but several discrepancies between the analytically-predicted and measured results are apparent. Notably, the analytic model predicted that the frequency of minimum reflection and the frequency of maximum polarization conversion efficiency would coincide at around 33 GHz. However, the fabricated device has the best measured conversion efficiency at around 38 GHz.

TABLE 2. Physical parameters for the Ka-band isotropic rotator.

Symbol	Parameter	Value
ϵ_1	Al_2O_3 permittivity	$9.7(1 - i10^{-4})$
ϵ_2	air permittivity	1
Λ	grating period	1100 μm
N	number of layers	9
d	overall thickness	10.0 mm
d_l	layer thickness	(1160, 1120, 1200, 920, 1240, 920, 1200, 1120, 1160) μm
f_l	layer filling fraction	(0.30, 0.65, 0.36, 0.38, 0.65, 0.38, 0.36, 0.65, 0.30)
θ_l	layer rotation	(0°, 30°, 60°, 30°, 62°, 93°, 64°, 93°, 124°)

C. DUAL-BAND LINEAR-TO-CIRCULAR POLARIZER

In high speed K/Ka-band satellite communications, separate uplink and downlink frequency bands use circularly-polarized waves with opposite handedness for each band. Consequently, there has been considerable interest in dual-band, dual-function linear-to-circular polarization converters [47], [48], [49], [50], [51], [52], [53], which would allow using linearly-polarized antennas or antenna arrays for both transmit and receive in a shared aperture. Numerous such polarization converters have been proposed based on multi-layer patterned metallic claddings [47], [48], [49], [50], [51], [52]. However, achieving high fractional bandwidth for both transmission efficiency and axial ratio seems to be elusive for these metasurface-based devices. A cascaded dielectric grating structure with a large number of layers (and thus many degrees of freedom) may provide one approach to increasing the operating bandwidth. Here, we attempt to design a dual band linear-to-circular polarizer with high transmissivity and polarization purity over the entire uplink (17.3 – 21.2 GHz) and downlink (27.5 – 31 GHz) satellite communication bands.

In the linear polarization basis, the relevant transmission parameters are given by:

$$\begin{pmatrix} E_{ex}^{+} \\ E_{ey}^{+} \end{pmatrix} = \boldsymbol{S}_{\mathbf{21}}^{\mathrm{LIN}} \begin{pmatrix} E_{0x}^{+} \\ E_{0y}^{+} \end{pmatrix} = e^{i\varphi} \begin{pmatrix} t_{xx} & t_{xy} \\ t_{yx} & t_{yy} \end{pmatrix} \begin{pmatrix} E_{0x}^{+} \\ E_{0y}^{+} \end{pmatrix} \tag{21}$$

where φ is an arbitrary constant phase shift. An ideal linear-to-circular polarizer that converts an incident x-polarization into transmitted left-handed circular polarization would have $t_{xx} = 1/\sqrt{2}$ and $t_{yx} = i/\sqrt{2}$. Alternatively, it is convenient to work directly in the circular polarized basis for the transmitted fields, using a linear-to-circular transmission matrix defined as follows:

$$\begin{aligned} \begin{pmatrix} E_{eL}^{+} \\ E_{eR}^{+} \end{pmatrix} &= \boldsymbol{S}_{\mathbf{21}}^{\mathrm{CP}} \begin{pmatrix} E_{0x}^{+} \\ E_{0y}^{+} \end{pmatrix} = e^{i\varphi} \begin{pmatrix} t_{Lx} & t_{Ly} \\ t_{Rx} & t_{Ry} \end{pmatrix} \begin{pmatrix} E_{0x}^{+} \\ E_{0y}^{+} \end{pmatrix} \\ &= \frac{1}{\sqrt{2}} \begin{pmatrix} 1 & i \\ 1 & -i \end{pmatrix} \boldsymbol{S}_{\mathbf{21}}^{\mathrm{LIN}} \begin{pmatrix} E_{0x}^{+} \\ E_{0y}^{+} \end{pmatrix} \end{aligned} \tag{22}$$

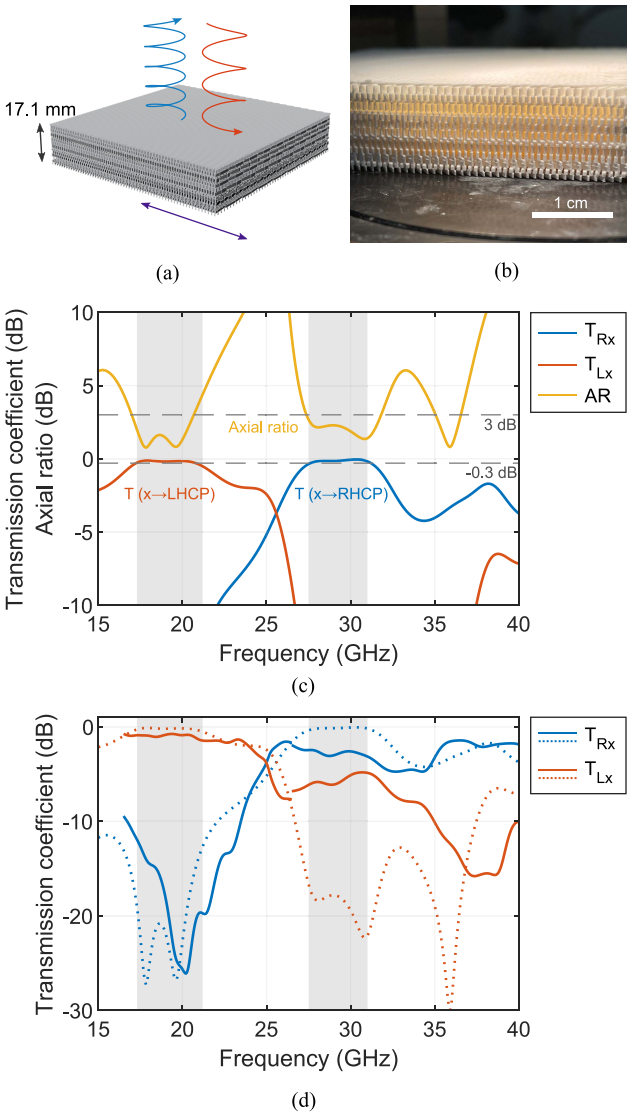

FIGURE 7. (a) Dual-band linear-to-circular polarizer design and illustration of operating characteristics. The polarizer converts linearly polarized incident waves upon transmission to left-hand circular polarization in the lower band and right-hand circular polarization in the upper band. (b) Fabricated device. (c) Calculated transmission coefficients and axial ratio using the analytic 4 × 4 matrix technique. The lower (17.3–21.2 GHz) and upper (27.5–31 GHz) operating bands are indicated in gray. Dotted lines show the optimization targets for the axial ratio (3 dB) and transmission coefficient (-0.3 dB). (d) Measured (solid) and calculated (dotted) transmission coefficients. The measurements were performed using different antennas and probes for the upper and lower frequency bands.

The ideal left-handed polarizer would then have $t_{Lx} = 1$ and $t_{Rx} = 0$ (or vice-versa for a right-handed polarizer). The transmitted wave's polarization purity can be expressed in terms of the axial ratio (AR), which is related to the linear-to-circular transmission matrix by [54]:

$$AR = \frac{|t_{Rx}/t_{Lx}| + 1}{|t_{Rx}/t_{Lx}| - 1} \tag{23}$$

Our goal was to achieve an axial ratio less than 3 dB and transmissivity greater than −0.3 dB over the entirety of both operating bands. The cost function to be minimized was

$$\text{cost} = \sum_{\text{band 1}} (1 - |T_{Lx}|)^2 + |T_{Rx}|^2 + 0.2|R_x|^2 + \sum_{\text{band 2}} (1 - |T_{Rx}|)^2 + |T_{Lx}|^2 + 0.2|R_x|^2 \tag{24}$$

where $T_{Lx} = |t_{Lx}|^2$, $T_{Rx} = |t_{Rx}|^2$, and $R_x = |r_{xx}|^2 + |r_{yx}|^2$ are the power transmissivity and reflectivity, respectively. Using alumina and air subwavelength gratings with the grating period fixed at $\Lambda = 1100\,\mu$m, the filling fraction f_l, layer thicknesses d_l, and optic axis rotation angles θ_l for each layer were numerically optimized to minimize this cost function for the analytically-predicted scattering parameters. The assumed number of layers was gradually increased until the performance goals were met for the entire uplink and downlink bands. The smallest optimized structure found that achieved the goals comprised 16 layers with a 17.1 mm total thickness. Table 3 summarizes the optimized physical parameters, while Fig. 7(a)-(c) show the fabricated device design and analytically-predicted performance.

TABLE 3. Physical parameters for the dual-band linear-to-circular polarizer.

Symbol	Parameter	Value
ϵ_1	Al_2O_3 permittivity	$9.7(1 - i10^{-4})$
ϵ_2	air permittivity	1
Λ	grating period	1100 μm
N	number of layers	16
d	overall thickness	17.1 mm
d_l	layer thickness	(960, 920, 1520, 1280, 1360, 560, 520, 1520, 1480, 1240, 520, 1520, 600, 1200, 1360, 520) μm
f_l	layer filling fraction	(0.30, 0.65, 0.36, 0.54, 0.30, 0.65, 0.65, 0.41, 0.42, 0.65, 0.30, 0.30, 0.46, 0.65, 0.30, 0.30)
θ_l	layer rotation	(126°, 96°, 138°, 104°, 74°, 104°, 134°, 83°, 53°, 83°, 113°, 80°, 50°, 83°, 53°, 18°)

To demonstrate the potential bandwidth improvement possible with a cascaded grating structure, Table 4 compares the example device's calculated performance to several recent patterned metallic designs reported in the literature. The simulated performance was used for each device, since experimental measurements were not always available. In Table 4, the bandwidth is defined as the frequency range over which the axial ratio is less than 3 dB and the transmission is greater than −1 dB. Thickness is expressed in free-space wavelengths at the center frequency of the lower band.

The fabricated device performance was measured using the probe-compensated near-field scanning technique, Fig. 4(c). Separate source antennas and waveguide probes were used for the Ku (18 – 26.5 GHz) and Ka (25.6 – 40 GHz) ranges. In particular, the lower band used a Ku-band standard gain horn with dual-lens focusing telescope along with a WR-42 rectangular waveguide probe; the upper band used a Gaussian

TABLE 4. Simulated performance comparison among K-band dual-band linear-to-circular polarizers.

	Lower Band (GHz)	Upper Band (GHz)	Relative Polarization	Thickness	Construction
[47]	19.2 – 20.3 (5.6%)	29.0 -- 31.0 (6.7%)	L/R	0.07λ	3 metal layers, dielectric spacers
[48]	18.8 -- 20.3 (7.7%)	28.9 — 30.3 (4.7%)	same	0.31λ	5 metal layers, dielectric spacers
[49]	18.5 -- 20.8 (12%)	27.0 — 29.3 (8.2%)	L/R	0.10λ	2 metal layers, dielectric spacers
[51]	17.4 -- 18.0 (3.4%)	26.5 -- 28.1 (5.9%)	L/R	0.06λ	3 metal layers, dielectric spacers
[52]	18.0 — 21.6 (18.2%)	28.8 — 30.6 (6.1%)	L/R	0.21λ	3 metal layers, dielectric spacers
This work	17.0 -- 20.7 (19.6%)	27.4 -- 31.8 (14.9%)	L/R	1.07λ	16 dielectric grating layers

optic horn antenna with integrated focusing lens (Millitech GOA-28) along with a WR-28 rectangular waveguide probe.

Fig. 7(d) shows the measured polarizer performance compared to the analytic predictions. While the dual-band linear-to-circular polarization behavior is qualitatively evident, significant deviations from the analytic predictions can be seen, including a large degradation of the transmitted axial ratio in the upper band.

VI. CONCLUSION

Additively-manufactured, cascaded, dielectric gratings are a promising and viable platform for polarization converters at microwave frequencies up to at least 40 GHz. In particular, ceramic structures such as alumina/air gratings fabricated using ceramic stereolithography have many appealing material properties including high dielectric contrast, low loss, chemical and weather resistance, and structural robustness. Additive manufacturing allows the structures to be precisely and monolithically fabricated without additional assembly steps. Finally, the high number of degrees of freedom in the multilayer cascaded grating structures affords significant flexibility to implement broadband, multiband, or multifunctional polarization conversion devices with no need for additional impedance matching layers.

However, analysis improvements are needed to enable effective device designs based on cascaded gratings. Full wave simulations for these structures can be prohibitively complex (and rigorous simulations based on periodic unit cells are generally impossible for three or more rotated cascaded gratings whose principle axes do not align). With appropriate homogenization assumptions, analytic techniques based on matrix methods can significantly speed up analysis and enable optimization. Unfortunately, as seen here with the isotropic rotator and linear-to-circular converter example devices, notable deviations between analytic and measured performance can arise for complicated devices with many layers. The most likely cause for these deviations is higher-order evanescent coupling between adjacent rotated grating layers, which was ignored in the homogenized analytic approach. Such coupling could introduce very small errors in the reflection and transmission phase between layers, which could become significant in complicated devices with many internal reflections. This suggests that one path forward could be to design devices with homogeneous spacers between adjacent grating layers, such as in [16], [55], which would reduce evanescent coupling.

REFERENCES

[1] S. Pancharatnam, "Achromatic combinations of birefringent plates," *Proc. Indian Acad. Sci. Sect. A*, vol. 41, no. 4, pp. 137–144, Apr. 1955.

[2] P. Yeh, *Optical Waves in Layered Media*. New York, NY, USA: Wiley, 1988.

[3] J.-B. Masson and G. Gallot, "Terahertz achromatic quarter-wave plate," *Opt. Lett.*, vol. 31, no. 2, pp. 265–267, Jan. 2006.

[4] G. Pisano, G. Savini, P. A. R. Ade, V. Haynes, and W. K. Gear, "Achromatic half-wave plate for submillimeter instruments in cosmic microwave background astronomy: Experimental characterization," *Appl. Opt.*, vol. 45, no. 27, pp. 6982–6989, Sep. 2006.

[5] M. Born and E. Wolf, *Principles of Optics: Electromagnetic Theory of Propagation, Interference and Diffraction of Light*, 7th ed. Cambridge, U.K.: Cambridge Univ. Press, 1999, ch. 15.5.2, pp. 837–840.

[6] D. C. Flanders, "Submicrometer periodicity gratings as artificial anisotropic dielectrics," *Appl. Phys. Lett.*, vol. 42, no. 6, pp. 492–494, Mar. 1983.

[7] P. Lalanne and D. Lemercier-Lalanne, "On the effective medium theory of subwavelength periodic structures," *J. Modern Opt.*, vol. 43, no. 10, pp. 2063–2085, Oct. 1996.

[8] H. Kikuta, Y. Ohira, H. Kubo, and K. Iwata, "Effective medium theory of two-dimensional subwavelength gratings in the non-quasi-static limit," *J. Opt. Soc. Amer. A, Opt. Image Sci.*, vol. 15, no. 6, pp. 1577–1585, Jun. 1998.

[9] H. Kikuta, Y. Ohira, and K. Iwata, "Achromatic quarter-wave plates using the dispersion of form birefringence," *Appl. Opt.*, vol. 36, no. 7, pp. 1566–1572, Mar. 1997.

[10] Y. Wu, P. S. Grant, and D. Isakov, "3D-printed λ/4 phase plate for broadband microwave applications," *Opt. Exp.*, vol. 26, no. 22, pp. 29068–29073, Oct. 2018.

[11] N. Castro, F. Pizarro, and E. Rajo-Iglesias, "High gain low profile horn array with circular polarization using a 3D printed anisotropic dielectric composite material at 38 GHz," *Sci. Rep.*, vol. 12, no. 1, Nov. 2022, Art. no. 18944.

[12] H. Shi and Y. Hao, "Wide-angle optical half-wave plate from the field transformation approach and form-birefringence theory," *Opt. Exp.*, vol. 26, no. 16, pp. 20132–20144, Aug. 2018.

[13] Y. Ono, Y. Kimura, Y. Ohta, and N. Nishida, "Antireflection effect in ultrahigh spatial-frequency holographic relief gratings," *Appl. Opt.*, vol. 26, no. 6, pp. 1142–1146, Mar. 1987.

[14] M. Kim and G. V. Eleftheriades, "Highly efficient all-dielectric optical tensor impedance metasurfaces for chiral polarization control," *Opt. Lett.*, vol. 41, no. 20, pp. 4831–4834, Oct. 2016.

[15] A. Ranjbar and A. Grbic, "Multifunctional all-dielectric metasurfaces," in *Proc. IEEE Int. Symp. Antennas Propag. USNC/URSI Nat. Radio Sci. Meeting*, Boston, MA, USA, Jul. 2018, pp. 1485–1486.

[16] A. Ranjbar and A. Grbic, "Broadband, multiband, and multifunctional all-dielectric metasurfaces," *Phys. Rev. Appl.*, vol. 11, no. 5, May 2019, Art. no. 54066.

[17] C. Pfeiffer and B. Tomasic, "Linear-to-circular polarizers for multi-octave bandwidths and wide scan angles at mm-wave frequencies using rotated anisotropic layers," *Progr. Electromagn. Res.*, vol. 79, pp. 49–64, Oct. 2017.

[18] M. L. Griffith and J. W. Halloran, "Freeform fabrication of ceramics via stereolithography," *J. Amer. Cerem. Soc.*, vol. 79, no. 10, pp. 2601–2608, Oct. 1996.

[19] G. A. Brady and J. W. Halloran, "Differential photo-calorimetry of photopolymerizable ceramic suspensions," *J. Mater. Sci.*, vol. 33, no. 18, pp. 4551–4560, Sep. 1998.

[20] G. A. Brady and J. W. Halloran, "Solid freeform fabrication of ceramics by stereolithography," *Nav. Res. Rev.*, vol. 50, pp. 39–43, Jan. 1998.

[21] G. T.-M. Chu, G. A. Brady, W. Miao, and J. W. Halloran, "Ceramic SFF by direct and indirect stereolithography," *MRS Online Proc. Library*, vol. 542, pp. 119–123, Feb. 2011.

[22] H. Liao and T. W. Coyle, "Photoactive suspensions for stereolithography of ceramics," *J. Can. Cerem. Soc.*, vol. 65, no. 4, pp. 254–262, Nov. 1996.

[23] J. H. Lee, R. K. Prud'homme, and I. A. Aksay, "Processing of organic/inorganic composites by stereolithography," *MRS Online Proc. Library*, vol. 625, p. 22, Nov. 2000.

[24] C. Hinczewski, S. Corbel, and T. Chartier, "Ceramic suspensions suitable for stereolithography," *J. Eur. Cerem. Soc.*, vol. 18, no. 6, pp. 583–590, Jan. 1998.

[25] O. Dufaud and S. Corbel, "Stereolithography of PZT ceramic suspensions," *Rapid Prototyping J.*, vol. 8, no. 2, pp. 83–90, May 2002.

[26] R. Felzmann et al., "Lithography-based additive manufacturing of cellular ceramic structures," *Adv. Eng. Mater.*, vol. 14, no. 12, pp. 1052–1058, 2012.

[27] G. Mitteramskogler et al., "Light curing strategies for lithography-based additive manufacturing of customized ceramics," *Additive Manuf.*, vols. 1–4, pp. 110–118, Oct. 2014.

[28] K. F. Brakora, J. Halloran, and K. Sarabandi, "Design of 3-D monolithic MMW antennas using ceramic stereolithography," *IEEE Trans. Antennas Propag.*, vol. 55, no. 3, pp. 790–797, Mar. 2007.

[29] P. Lalanne, S. Astilean, P. Chavel, E. Cambril, and H. Launois, "Blazed binary subwavelength gratings with efficiencies larger than those of conventional échelette gratings," *Opt. Lett.*, vol. 23, no. 14, pp. 1081–1083, Jul. 1998.

[30] D. Isakov, Y. Wu, B. Allen, P. S. Grant, C. J. Stevens, and G. J. Gibbons, "Evaluation of the Laguerre–Gaussian mode purity produced by three-dimensional-printed microwave spiral phase plates," *Roy. Soc. Open Sci.*, vol. 7, no. 7, Jul. 2020, Art. no. 200493.

[31] D. W. Berreman, "Optics in stratified and anisotropic media: 4×4-matrix formulation," *J. Opt. Soc. Amer.*, vol. 62, no. 4, pp. 502–510, Apr. 1972.

[32] P. Yeh, "Electromagnetic propagation in birefringent layered media," *J. Opt. Soc. Amer.*, vol. 69, no. 5, pp. 742–756, May 1979.

[33] N. C. Passler and A. Paarmann, "Generalized 4 × 4 matrix formalism for light propagation in anisotropic stratified media: Study of surface phonon polaritons in polar dielectric heterostructures," *J. Opt. Soc. Amer. B, Opt. Phys.*, vol. 34, no. 10, pp. 2128–2139, Oct. 2017.

[34] A. Ranjbar and A. Grbic, "Analysis and synthesis of cascaded metasurfaces using wave matrices," *Phys. Rev. B, Condens. Matter*, vol. 95, no. 20, May 2017, Art. no. 205114.

[35] M. N. Afsar and K. J. Button, "Precise millimeter-wave measurements of complex refractive index, complex dielectric permittivity and loss tangent of GaAs, Si, SiO_2, Al_2O_3, BeO, Macor, and glass," *IEEE Trans. Microw. Theory Techn.*, vol. MTT-31, no. 2, pp. 217–223, Feb. 1983.

[36] J. Krupka, K. Derzakowski, B. Riddle, and J. Baker-Jarvis, "A dielectric resonator for measurements of complex permittivity of low loss dielectric materials as a function of temperature," *Meas. Sci. Technol.*, vol. 9, no. 10, p. 1751, Oct. 1998.

[37] P. F. Goldsmith, "Quasi-optical techniques," *Proc. IEEE*, vol. 80, no. 11, pp. 1729–1747, Nov. 1992.

[38] S. M. Rudolph, C. Pfeiffer, and A. Grbic, "Design and free-space measurements of broadband, low-loss negative-permeability and negative-index media," *IEEE Trans. Antennas Propag.*, vol. 59, no. 8, pp. 2989–2997, Aug. 2011.

[39] A. Yaghjian, "An overview of near-field antenna measurements," *IEEE Trans. Antennas Propag.*, vol. AP-34, no. 1, pp. 30–45, Jan. 1986.

[40] J. J. H. Wang, "An examination of the theory and practices of planar near-field measurement," *IEEE Trans. Antennas Propag.*, vol. 36, no. 6, pp. 746–753, Jun. 1988.

[41] M. S. Gatti and Y. Rahmat-Samii, "FFT applications to plane-polar near-field antenna measurements," *IEEE Trans. Antennas Propag.*, vol. 36, no. 6, pp. 781–791, Jun. 1988.

[42] S. Young, L. Szymanski, and A. Grbic, "Broadband dielectric metasurfaces using ceramic stereolithography," in *Proc. 13th Int. Congr. Artif. Mater. Novel Wave Phenom. (Metamaterials)*, Rome, Italy, Sep. 2019, pp. 483–485.

[43] S. Young, L. Szymanski, and A. Grbic, "Metastructures consisting of cascaded high-contrast subwavelength gratings," in *Proc. High Contrast Metastruct. IX*, San Francisco, CA, USA, Feb. 2020, Art. no. 112900Z.

[44] A. V. Rogacheva, V. A. Fedotov, A. S. Schwanecke, and N. I. Zheludev, "Giant gyrotropy due to electromagnetic-field coupling in a bilayered chiral structure," *Phys. Rev. Lett.*, vol. 97, no. 17, Oct. 2006, Art. no. 177401.

[45] C. Pfeiffer and A. Grbic, "Bianisotropic metasurfaces for optimal Polarization control: Analysis and synthesis," *Phys. Rev. Appl.*, vol. 2, no. 4, Oct. 2014, Art. no. 44011.

[46] C. Pfeiffer, C. Zhang, V. Ray, L. J. Guo, and A. Grbic, "Polarization rotation with ultra-thin bianisotropic metasurfaces," *Optica*, vol. 3, no. 4, pp. 427–432, Apr. 2016.

[47] P. Naseri, S. A. Matos, J. R. Costa, C. A. Fernandes, and N. J. G. Fonseca, "Dual-band dual-linear-to-circular polarization converter in transmission mode application to *K*/*Ka*-band satellite communications," *IEEE Trans. Antennas Propag.*, vol. 66, no. 12, pp. 7128–7137, Dec. 2018.

[48] M. Hosseini and S. V. Hum, "A systematic circuit-based approach to efficiently realize single- and dual-band circular polarizers," in *Proc. 12th Eur. Conf. Antennas Propag. (EuCAP)*, Apr. 2018, pp. 1–5.

[49] H. B. Wang and Y. J. Cheng, "Single-layer dual-band linear-to-circular polarization converter with wide axial ratio bandwidth and different polarization modes," *IEEE Trans. Antennas Propag.*, vol. 67, no. 6, pp. 4296–4301, Jun. 2019.

[50] A. K. Fahad, C. Ruan, and K. Chen, "Dual-wide-band dual polarization terahertz linear to circular polarization converters based on bi-layered transmissive metasurfaces," *Electronics*, vol. 8, no. 8, p. 869, Aug. 2019.

[51] P. Naseri, J. R. Costa, S. A. Matos, C. A. Fernandes, and S. V. Hum, "Equivalent circuit modeling to design a dual-band dual linear-to-circular polarizer surface," *IEEE Trans. Antennas Propag.*, vol. 68, no. 7, pp. 5730–5735, Jul. 2020.

[52] M. Del Mastro, M. Ettorre, and A. Grbic, "Dual-band, orthogonally-polarized LP-to-CP converter for SATCOM applications," *IEEE Trans. Antennas Propag.*, vol. 68, no. 9, pp. 6764–6776, Sep. 2020.

[53] J.-N. Wang, Z.-J. Guo, and Z.-C. Hao, "A millimeter-wave planar dual-band array antenna having individually LHCP and RHCP radiation characteristics," *IEEE Open J. Antennas Propag.*, vol. 3, pp. 768–773, 2022.

[54] C. A. Balanis, *Antenna Theory: Analysis and Design*, 4th ed. Hoboken, NJ, USA: Wiley, 2016.

[55] A. Ranjbar, M. Jafari, M. Rais-zadeh, and A. Grbic, "All-dielectric metasurfaces for multifunctional polarization control," presented at the Int. Workshop Antenna Technol. (iWAT), Miami, FL, USA, Mar. 2019.